ADVANCED FUNCTIONAL MATERIALS
www.afm-journal.de

Chitosan-Decorated Alumina Hybrid Nanoparticles as Smart Scavengers of HF and Dissolved Transition Metals in Lithium-Ion Batteries

*Daniele Callegari, Mattia Canini, Stefania Davino, Mauro Coduri, Piercarlo Mustarelli, and Eliana Quartarone**

Lithium-ion cells encompassing $LiPF_6$ as the lithium salt and high-voltage ($LiNi_{0.5}Mn_{1.5}O_4$, LNMO) or high-capacity ($LiNi_{0.8}Mn_{0.1}Co_{0.1}O_2$, NMC811) cathode materials are prone to transition metal (TM) dissolution caused by HF, whose formation is catalyzed by H_2O traces. TM ions can shuttle to the anodic compartment, increasing the cell degradation rate. Accordingly, specific self-healing strategies are helpful to develop scavengers able to eliminate HF and absorb TM ions so avoiding their shuttling. In this work, the fabrication and test of a bi-functional, autonomous scavenging agent made of Al_2O_3 particles decorated is reported with chitosan. The nanometric Al_2O_3 core is a trap for HF by chemical bonding. The chitosan coating is acid-sensitive, and the opening of such a capping layer is triggered in the presence of even small amounts of HF, leading to an efficient TM ion-trapping. In addition, chitosan is biocompatible, biodegradable, and abundant, which is relevant for design-for-recycling scopes. With ≈200 ppm of water in the electrolyte, 12 wt% of scavenger causes, after 200 cycles at 1C, an increase of capacity retention from 73% to 88% for LNMO, and, impressively, from 46% to 84% for NMC811. This autonomous self-healing mechanism is promising for application in next-generation smart cells without requiring any external sensing.

1. Introduction

The rapid development of electric vehicles requires to improve lithium-ion battery technology to achieve high-capacity, long-lasting, and cost-effective devices. The cathode compartment plays a crucial role in determining the cost and performance of these batteries. Recently, Ni-rich cathode materials, with spinel or layered structures, have become increasingly popular due to their high capacity, excellent rate performance, and relatively low toxicity.[1–3] $Li_{0.5}Mn_{1.5}O_4$ (LMNO) is one of the most promising cathode materials thanks to its high-voltage operating conditions. However, its practical application is limited due to the chemical dissolution of Mn into the spinel. The process is accelerated at higher temperatures and in case of water impurities making slightly acidic the electrolyte.[4] This results in a disproportionation reaction of extensively lithiated particles with high Mn(III) concentration, leading to the formation of Mn(IV) in the solid active materials and Mn(II) ions being released in the electrolyte.[5] The dissolved Mn ions then migrate to the anode through chemical crosstalk, where they are reduced to metallic Mn enhancing the electrode polarization. Additionally, the Mn ions react with the SEI resulting in a consumption of Li cations and the formation of high resistance passivation layer that inhibits Li diffusion.[6]

In the case of layered oxides, ideally, Mn in the lattice should be stable without undergoing dissolution. In contrast, transition metals (TMs) leaching is observed also for most layered NMC oxides.[7] Here, the dissolution of TMs in presence of acidic electrolyte takes place through an even more complex mechanism involving a multi-step process: i) charge compensation of TMs by Li deintercalation accompanied by release of O_2, defects formation and Ni(II) ions leaching, and ii) consequent disproportionation reaction of manganese that causes the enrichment in Mn on the particle surface.[8] This mechanism is responsible of the irreversible structural and compositional evolution of the cathode upon cycling. In both systems, such degradation processes lead to a significant increase of cell impedance, the promotion of parasitic reactions as well as to severe

D. Callegari, M. Canini, S. Davino, M. Coduri, E. Quartarone
Department of Chemistry
University of Pavia
Via Taramelli 16, Pavia 27100, Italy
E-mail: eliana.quartarone@unipv.it
D. Callegari, P. Mustarelli, E. Quartarone
GISEL – Centro di Riferimento Nazionale per i Sistemi di Accumulo Elettrochimico di Energia
INSTM
via G. Giusti 9, Firenze 50121, Italy
P. Mustarelli
Dept. of Materials Science
University of Milano Bicocca
Via Cozzi 55, Milano 20121, Italy

The ORCID identification number(s) for the author(s) of this article can be found under https://doi.org/10.1002/adfm.202406315

DOI: 10.1002/adfm.202406315

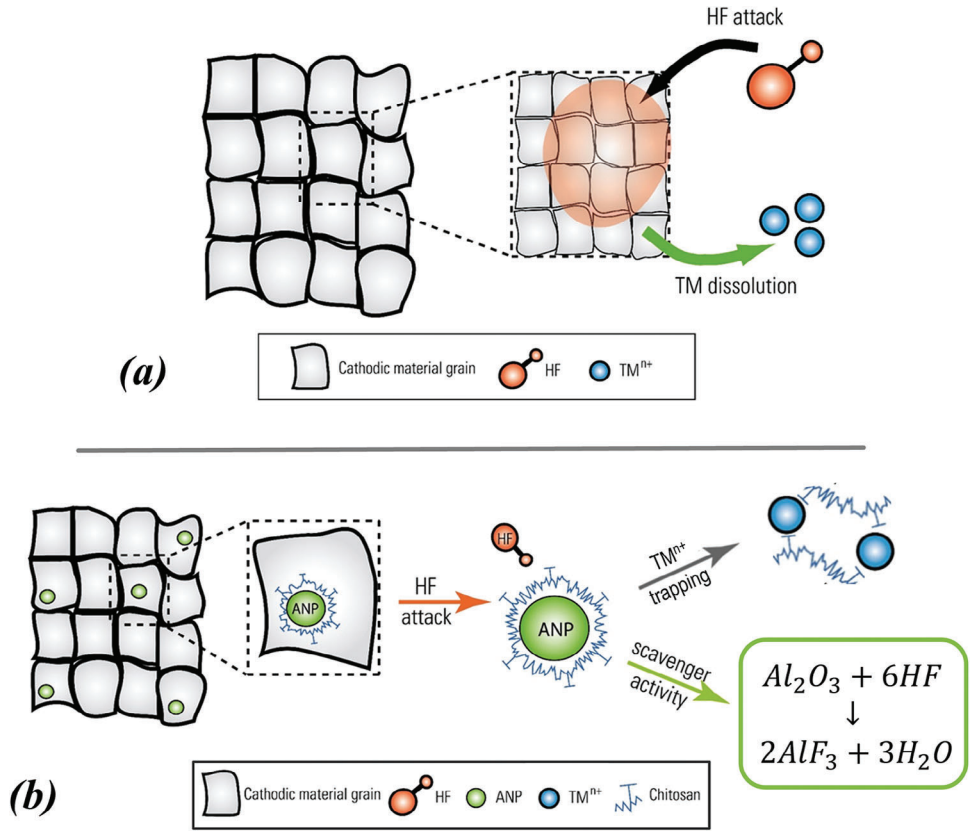

Figure 1. a) Transition metals leaching due to HF attack, and b) concept of the HF scavenger design.

capacity decay. The consequent reduction of the overall cell lifetime makes still challenging the use of high voltage and high energy density cathodes, overall, in case of fluorinated-based electrolytes.[9–14]

Indeed, the TMs dissolution from the cathode active materials is triggered by corrosive processes caused by the decomposition of the electrolyte salt.[6] Previous studies reported on a significant increase of TM ions leaching in case of $LiPF_6$-based electrolytes. This observation confirmed that even small traces of water are enough to generate significant amounts of hydrofluoric acid (HF) from the autocatalytic $LiPF_6$ decomposition though the following steps: $LiPF_6 \rightarrow LiF + PF_5$; ii) $PF_5 + H_2O \rightarrow POF_3 + 2HF$.[15]

To prevent or mitigate the detrimental instability of these cathode active materials, several strategies have been recently proposed in literature,[16] for example: i) the engineering of special additives for the liquid electrolytes,[17,18] such as organic Lewis bases or units with high electron donating ability (e.g., aminosilane);[19,20] ii) the doping of the cathode active materials (e.g., by means of Al(III) ions),[21] and iii) the electrode surface coating with artificial layer to avoid metal dissolution. Several studies also reported on the functionalization of smart separators including chelating agents (e.g., crown ethers-based systems),[22] capable to trap the dissolved TM ions and provide effective control on the crosstalk process with consequent stabilization of the SEI and enhanced cell lifetime.

Another promising strategy is the use of additives with scavenging properties toward the molecules released by decomposition reactions (e.g., H_2O, O_2, HF). These additives are usually dispersed as fillers in smart separators or deposited as coating layers onto the cathode surface.[23] They act as a chemical barrier against impurities and are capable to prevent their damaging effect on the cell performances. Different scavengers were investigated, both organic structures with different functionalities (e.g., COF, MOF, crown-ethers, cyclodextrins, etc),[24] as well as inorganic systems, such as metal oxides, phosphates, fluorides, or even silicate-based glasses.[25–28] Promising results were also achieved by means of cathode coating with metal oxides (e.g., Al_2O_3, ZrO_2, TiO_2 and silicate glasses), which appear to be particularly effective as HF scavengers.[29–33] Thanks to their high chemical resistance against acidic environment and absorbent properties, they bind fluorine, thus avoiding corrosive attack on the cathode active material.[34] The coating layers are assumed to be poorly reactive with the fluorine-based electrolyte, thermally resistant and electrochemically stable in the voltage operating range.

However, the use of the inorganic scavengers as cathode coatings faces some issues. First, they are deposited as uniform and dense film that can result in high impedance, since such oxides are poor ionic and electronic conductors. Additionally, the cathode particles undergo volumetric changes upon lithiation/delithiation, exerting strain on the coating with consequent

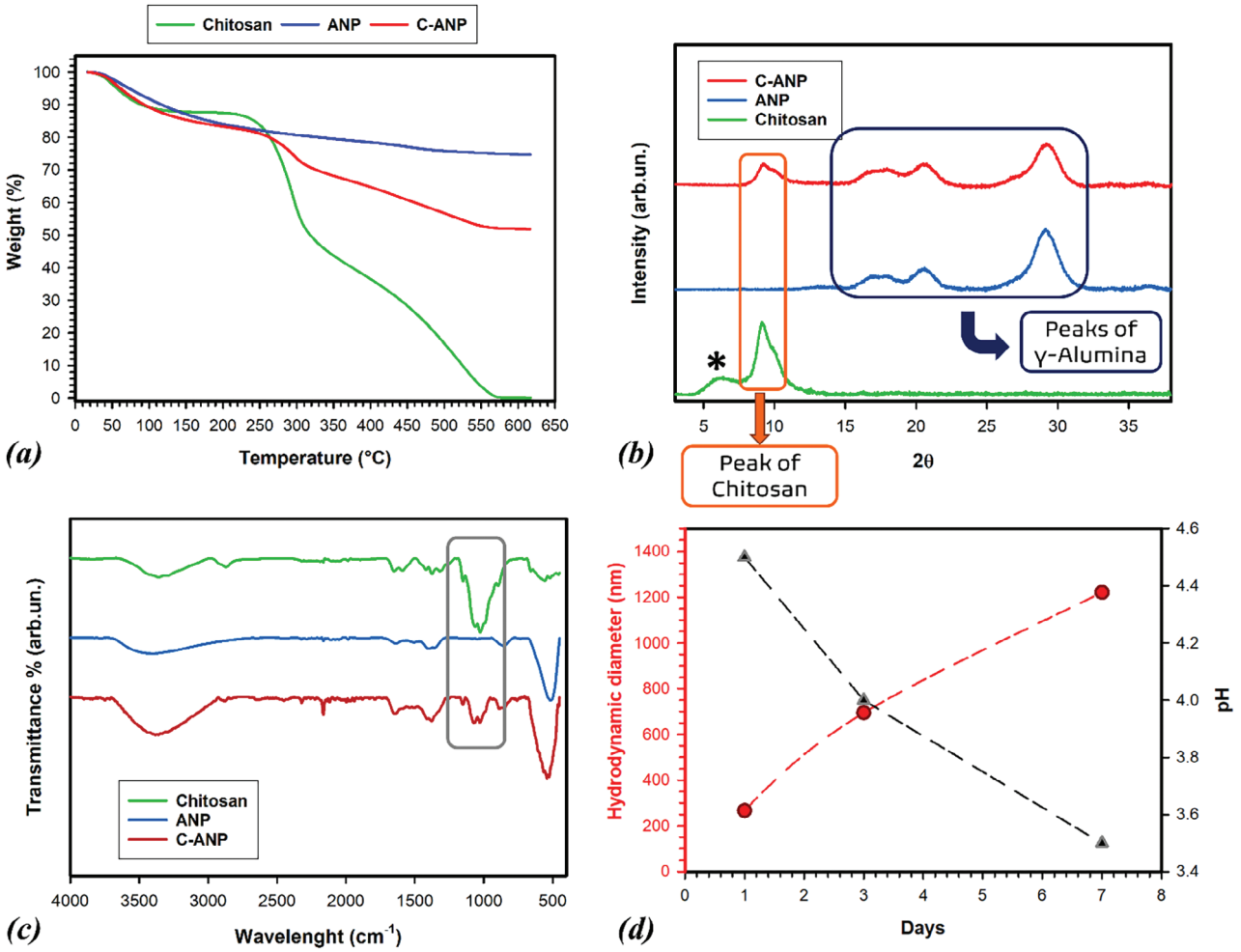

Figure 2. a)TGA plots, b) XRD patterns (Mo source), and c) FTIR spectra of alumina nanoparticles (ANP) (blue), chitosan (green) and functionalized alumina nanoparticles (C-ANP) (red). d) Hydrodynamic diameters evolution of C-ANPs over time in LP30 electrolyte at 55 °C, together with the evolution of pH with time due to HF generation.

generation of cracks and mechanical damage.[35] Therefore, a rational design of cathodes including scavenging functionalities is still needed to develop safe and long-lasting Li-ion cells based on spinel- and layered-based chemistries.

In this study we demonstrate the multifunctional activity of chitosan-functionalized alumina nanoparticles (C-ANP) capable of acid scavenging and TMs ion trapping to enhance the performance and the safety of LNMO and NMC811 ($LiNi_{0.8}Mn_{0.1}Co_{0.1}O_2$)-based LIBs. The hybrid material was used as a nanofiller homogenously dispersed in the cathode. Aggressive experimental conditions were used to trigger the metals dissolution and the chemical crosstalk toward the anode by adding large and controlled amount of water in the electrolyte.

2. Results and Discussion

2.1. Functional Design of the HF and TM Scavenger

The scavenger has been designed to put together three well-defined functionalities and properties:

i. A core component, namely Al_2O_3, as a trap for HF by means of chemical bonding. This component is nanometric to increase the surface available to the reaction and allow a homogenous dispersion of the filler over the cathode. Alumina and other oxides, such as ZnO, are Lewis' acids that can neutralize trace amounts of HF by means of the reaction proposed in **Figure 1**, suppressing the cathode corrosion. The water generated by the reaction may be absorbed by the alumina particles while the aluminium fluoride, that is insoluble in the electrolyte, can potentially act as an additional chemical barrier against corrosive processes.[36,37]
ii. The functionalising unit, namely the chitosan-based moieties, as a strong agent for TM ion-trapping capability. Chitosan is a linear polysaccharide, with high environmental benignity due to its low toxicity, biocompatibility, biodegradability, and natural abundance. Its excellent adsorption properties, responsible for the high capability of metals recovery from solutions, are due to the relatively large surface area (favoured by the nanosized particle), the presence of hydroxyl groups, high activity for the chelation of metal

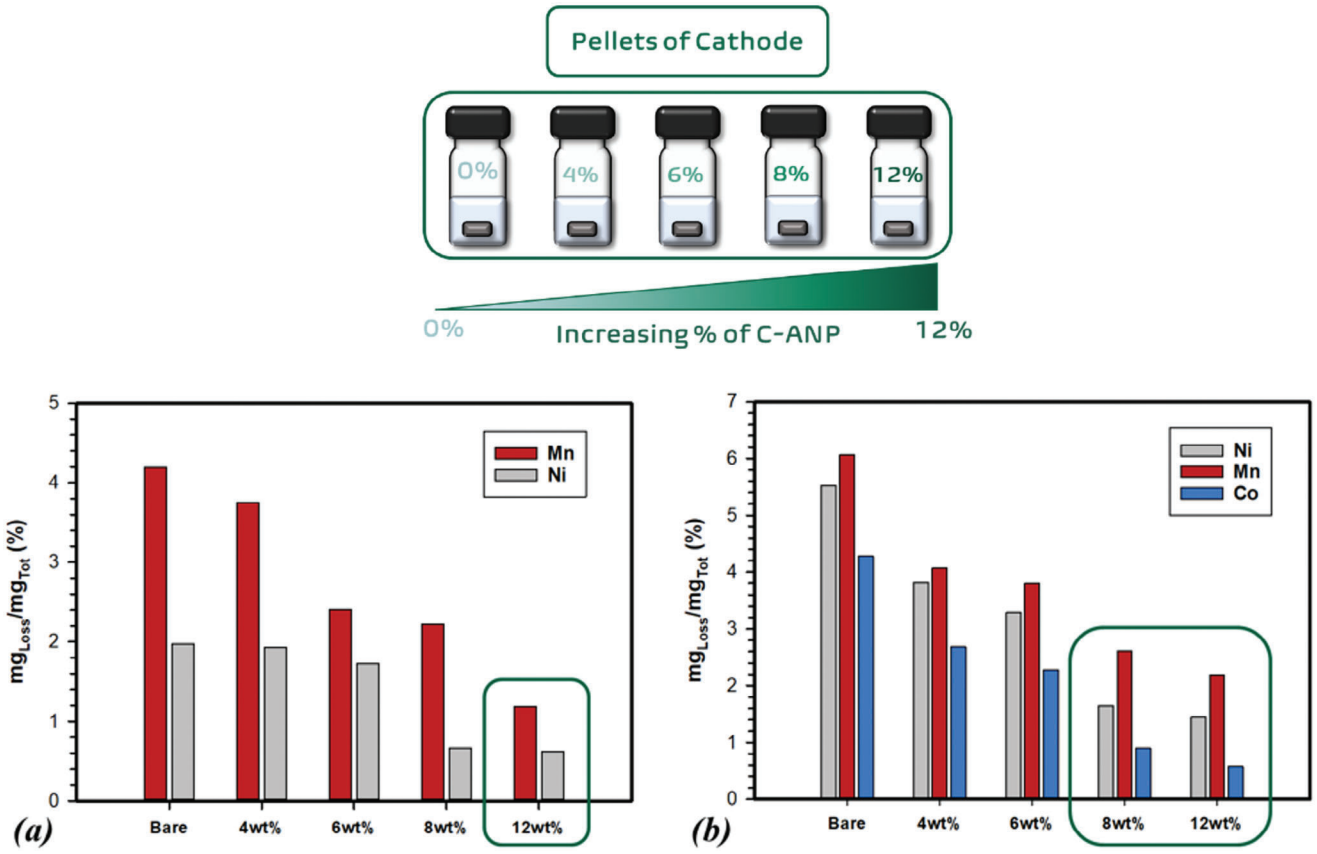

Figure 3. Quantification by ICP analysis of dissolved transition metal percentages for a) LNMO and b) NMC pellets at increasing wt% of C-ANP.

ions thanks to the presence of amino- groups, and flexible structure allowing to adopt suitable configuration for the metal ion complexation.[38] Functionalization of silica with chitosan-based systems were used, for example, as hybrid materials with high adsorption affinity for scandium to selectively recover the metal from aqueous solutions containing other metallic components.[39]

iii. The capping of the alumina core performed by chitosan, to entirely cover the inorganic particles surface. Such a coating is acid-sensitive,[40] and its opening is triggered on-demand in presence of even small amounts of acid. This mechanism makes this hybrid material suitable for the development of sensing/self-healing coupled smart functionalities for safer and durable LIBs.[41]

The effective alumina functionalization was evaluated by means of thermogravimetry, XRD and FTIR spectroscopy on deeply washed samples. Figure S1a (Supporting Information) shows the XRD pattern of the synthesised Al_2O_3 that can be indexed with the γ-Al_2O_3 phase, (space group *C2/m*), even though we cannot exclude the coexistence of other polymorphs considering the low-symmetry of the main phase and its limited crystallographic coherence.[42] The diffractogram clearly evidences the broad peaks consistent with the desired nanostructure, from which crystallite size of ≈5 nm can be determined by applying the Scherrer equation. SEM analysis, reported in Figure S1b (Supporting Information), further confirms the alumina nano-dimensioned structure, consisting of well-interconnected network of particles with average diameter ~50 nm.

The TGA plot, reported in **Figure 2a**, reveals a weight loss in the C-ANP sample of ≈20%, followed by degradation 30 °C higher than the pristine chitosan one. The higher degradation temperature of C-ANPs is an indirect evidence of chitosan bonding to the alumina surface. Figure 2b compares the diffractogram of C-ANP to the pure precursors, namely Al_2O_3 and chitosan. The pattern of the pristine polysaccharide exhibited the characteristic features assigned to the crystal forms I and II. In case of C-ANPs, the diffractogram shows the presence of the main peaks of both Al_2O_3 (highlighted in dark blue) and chitosan (highlighted in orange). Interestingly, the lower-angle peak characterising the polymer structure (highlighted by "*") disappears in the C-ANPs plot and this supports the bonding of the polymer to the alumina nanoparticles by means of hydrogen bonds between the chitosan amino groups and —OH groups on the alumina surface. Indeed, the suppression of this peak has been discussed in literature in terms of reduction of the intermolecular hydrogen bonds in the polysaccharide in a consequence of reactive processes.[43] Further evidence of the presence of chitosan onto the alumina particles is provided by the comparison of the FTIR spectra reported in Figure 2c. The spectrum of the C-ANP hybrid material exhibits the main bands of the original chitosan, assigned as in the following: i) a wide signal between 3600 and 3000 cm^{-1} describing the stretching vibration of O—H and N—H followed by the less intense band of the C—H symmetric and stretching ≈2900 cm^{-1};

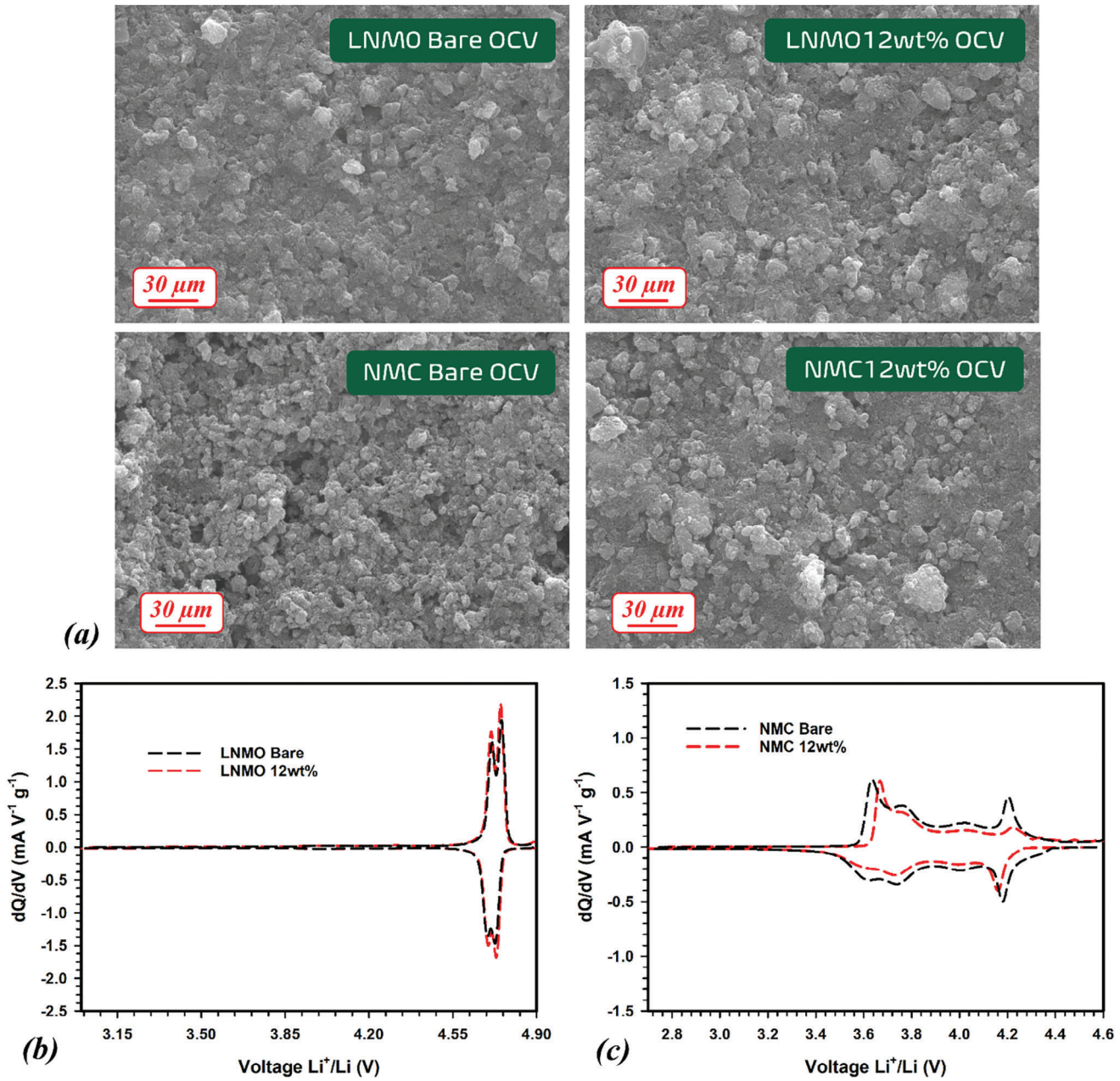

Figure 4. a) SEM images of LNMO (up) and NMC811 (down) cathodes before the electrochemical tests; dQ/dV plots of the 2nd Cycle of b) LNMO- and c) NMC-based by means of PCGA experiments at C/15.

2) smaller bands at 1640 and 1320 cm^{-1} due to the amide group related to the presence of residual N-acetyl groups and, finally, the more intense bands peaked ≈1000 cm^{-1} assigned to the C—O—C and C—O ether-based groups.

2.2. Evaluation of the Scavenger Activity of C-ANP

The acid sensitivity of the chitosan-functionalised alumina was evaluated by means of DLS measurements over time carried out on C-ANPs dispersed in the liquid electrolyte (LP30) at 55 °C to accelerate the electrolyte decomposition and the HF generation. Figure S2 (Supporting Information) reports the particle size distribution collected for the C-ANPs at t = 0 (just dispersed in the liquid electrolyte) and after 3 and 7 days, showing only one population within the sample. Figure 2d shows the hydrodynamic diameters versus time, which is related to the decrease of the pH due to continuous HF generation caused by the complex cascade mechanism of the $LiPF_6$ decomposition.[44] A hydrodynamic diameter of 287 nm was determined on the functionalized alumina, larger than the pristine Al_2O_3 (namely 50 nm) which further confirms the successful capping of the nanoparticles. The

particle dimensions rapidly increased with time up to diameters higher than 1200 nm, that makes evident the gradual opening of the capping chitosan layer of the alumina particles triggered by the presence of HF.

To assess the HF scavenging capability of the C-ANPs before their use in a real cell, pellets of both LNMO and NMC811 were immersed in a known volume of electrolyte and treated for 5 days at 55 °C to promote the CAM corrosion, leading to the dissolution of Mn, Ni and Co ions. Different quantities of C-ANPs were checked to find the minimal amount sufficient to effectively suppress a slow but continuous degradation process. **Figure 3** shows the amount of transition metals leached in the liquid electrolyte, measured by ICP-OES analysis for both the CAMs, mixed with different amounts of C-ANPs in the range 0–12 wt%.

In case of LNMO spinel (Figure 3a), the Mn leaching rate decreases almost linearly by increasing the amount of scavenger, whereas the Ni dissolution is stabilized at C-ANPs amounts higher than 6 wt%. Similar linear trends are observed for the layered NMC811 (Figure 3b), even if the control on the metal dissolution is significant also in presence of smaller scavenger concentrations. 12 wt% of C-ANPs was selected as the optimal composition for both the chemistries, which allows a decrease of the TM loss with respect to the scavenger-free sample (Bare cathode) of a factor of 3 for Mn and Ni for both LNMO and NMC. The scavenging activity of the filler is even more effective in case of Co in the layered system, whose leaching rate is significantly decreased (up 5 times) at scavenger concentration higher than 8 wt%.

Figure 4a shows SEM images of the LNMO and NMC811 cathodes, both Bare and composite including 12 wt% of C-ANPs, before the electrochemical tests (at OCV). The particles of both systems look morphologically similar, even if the NMC grains seem to be smaller.

First, it was evaluated whether the presence of the scavenger within the electrode could lead to undesired irreversible phenomena or alteration of redox processes (Figures S3, Supporting Information). Figure 4b compares the differential capacity plots of the 2nd cycle obtained by PCGA technique for the Bare cathodes and those including the C-ANP filler (12wt%), showing the typical redox processes expected for LNMO and NMC.[45,46] The C-ANP-based cathodes exhibit similar signals of intercalation/deintercalation and phase transitions as the pristine ones do, with no or very low voltage hysteresis, except for the NMC-based cell, whose peak at ≈3.7 V is slightly shifted at higher potential in case of scavenging cathode (NMC 12wt%). This confirms that, despite its insulating properties, the presence of 12% filler is not an obstacle to the electrical pathways of the electrode that still preserves its conductive network. This has been also observed in literature in case of alumina coated $LiCoO_2$ cathodes.[47]

To accelerate the cathode degradation and the leaching of the transition metals, electrolytes with well-defined water contamination levels were used to assemble the cell. In more detail, two different liquid electrolytes were considered depending on the cathode: LP30 in the case of LNMO and LP71 in the case of NMC811, whose final water contents (following water addition) were 170 and 225 ppm, respectively. The cycling stability of the cells with the scavenging cathodes (12 wt% LNMO and NMC) were compared to those obtained for cells with the corresponding Bare cathodes, herein considered as the baseline. **Table 1** reports the details of pristine and water-enriched electrolytes.

Table 1. Cell parameters computed in different conditions for LNMO and NMC cathodes and LNMO and NMC stoichiometry after 200 cycles at 1C, determined by ICP-OES analysis.

LNMO			
	spinel *a*/Å	rock salt *a*/Å	residual coefficients
Bare OCV	8.1659(2)	4.148(1)	$LiNi_{0.5}Mn_{1.5}O_4$
Bare (LP30)	8.1675(2)	4.149(2)	$LiNi_{0.48}Mn_{1.42}O_4$
Bare (LP30_E)	8.1658(2)	4.145(2)	$LiNi_{0.46}Mn_{1.36}O_4$
12wt% C-ANP OCV	8.1667(2)	4.146(2)	$LiNi_{0.5}Mn_{1.5}O_4$
12wt% C-ANP (LP30)	8.1684(2)	4.146(2)	$LiNi_{0.48}Mn_{1.44}O_4$
12wt% C-ANP (LP30_E)	8.1654(2)	4.142(1)	$LiNi_{0.48}Mn_{1.42}O_4$

NMC			
	layered *a*/Å	layered *c*/Å	residual coefficients
Bare OCV	2.8729(2)	14.205(1)	$LiNi_{0.8}Mn_{0.1}Co_{0.1}O_2$
Bare 200 (LP71)	2.8779(4)	14.238(1)	$LiNi_{0.73}Mn_{0.091}Co_{0.1}O_2$
Bare 200 (LP71_E)	2.8809(6)	14.223(1)	$LiNi_{0.69}Mn_{0.086}Co_{0.1}O_2$
12wt% C-ANP OCV	2.8717(2)	14.203(1)	$LiNi_{0.8}Mn_{0.1}Co_{0.1}O_2$
12wt% C-ANP 200 (LP71)	2.8800(2)	14.241(1)	$LiNi_{0.077}Mn_{0.098}Co_{0.1}O_2$
12wt% C-ANP (LP71_E)	2.8782(2)	14.228(1)	$LiNi_{0.76}Mn_{0.095}Co_{0.1}O_2$

Figures 5a,b compare the cycling performance at 1C and 25 °C of the LNMO and NMC cells, respectively. In both cases, the scavenging cathodes cells exhibit significantly higher discharge capacity retention and higher coulombic efficiency (>99.0%) (the latter one shown in Figure S4 (Supporting Information) which also reports the charge capacity values) than the Bare samples, also in case of water-free electrolytes, with the following sequence: LNMO > NMC. Significant improvements in the cycling performance are still more evident, especially in the presence of water-contaminated electrolytes (LP30_E and LP71_E). In this case, the presence of C-ANP contributes to maintain a higher capacity retention after 200 cycles than the Bare samples, namely 88% versus 73% for LNMO and 84% versus 46% in the case of NMC. In the latter case, the scavenging effect is even more impressive, taking into consideration the higher water amount in the LP71_E electrolyte. Throughout the cycling process, a stable capacity behaviour is observed that is superimposable to the values detected in case of water-free electrolyte, very close to the theoretical target.

This beneficial trend of the HF scavenger is also confirmed by the concentration of dissolved TMs measured at the anode after the long-term cycling test. As shown in Figures 5c,d, the addition of the functionalized alumina nanoparticles in both the cathodes leads to an overall reduction of the metal leaching. The impact of the HF scavenger is enhanced in the presence of water-enriched electrolytes (LP30_E and LP71_E) and is superior for NMC compared to the spinel cathode, in agreement with the literature.[48] In case of C-ANPs-based LNMO cathode, the Mn and Ni dissolution rates are almost halved with respect to the baseline, achieving values comparable to those obtained in case of water-free electrolytes (LP30 and LP71). In the C-ANPs-based NMC cells, a significant reduction of Ni and Mn leaching of a factor of 2.5 and 4, respectively, is observed after 200 cycles in case of LP71 electrolyte

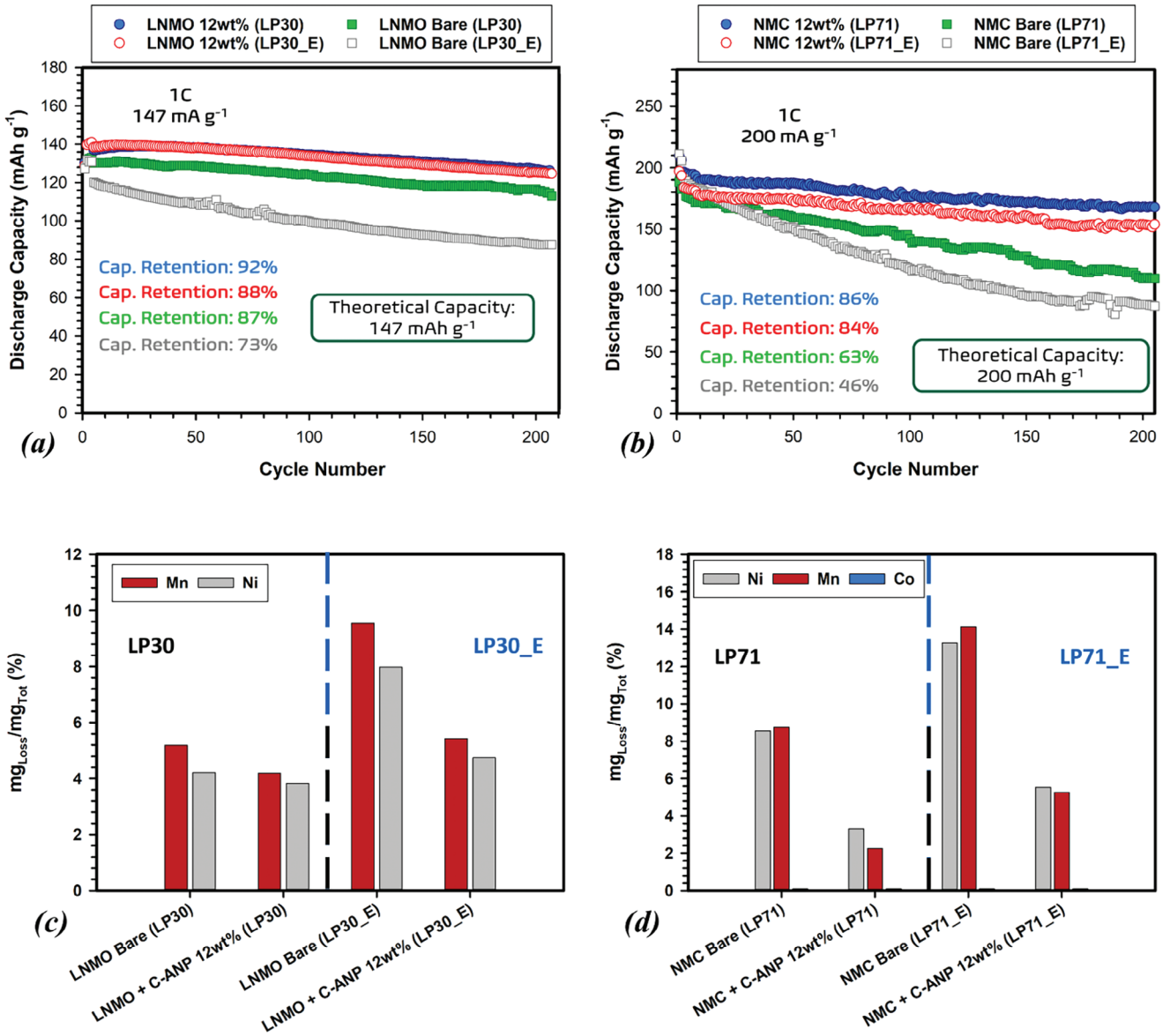

Figure 5. a,b) Long-term cycling at 1C for the LNMO cells (current density of 146.7 mA g^{-1}) and NMC cells (current density 200 mA g^{-1}) with and without C-ANP. Capacity retention was calculated between cycle 4 and 204. c,d) TMs concentration detected at the anode after the long-term cycling for all the investigated cells. No cobalt was detected by ICP analysis.

(no water added) and almost comparable effects are evident also in presence of water-contaminated electrolyte (LP71_E). Contrary to Ni and Mn, Co appears not to be affected by corrosive phenomena (Figure 5d). Additionally, the evaluation of voltage profiles for both cathode materials (illustrated in Figure S5, Supporting Information) reveals no significant differences in any of the cases analyzed, irrespective of the presence of C-ANPs and the use of a pristine or water-enriched electrolyte.

Figures 6a,b compare the impedance spectra collected after 200 cycles for all the investigated samples, namely the Bare cathodes and the C-ANP ones (12 wt%) with the pristine (LP30, LP71) and water-added electrolytes (LP30_E, LP71_E). The spectra were simulated by means of the equivalent circuits reported in the figure inset to determine the cell interfacial resistance, R_{CT}. Despite a 3-electrode configuration should be the right choice for a better identification of the interfacial phenomena, the following qualitative aspects can be highlighted anyway: i) the NMC cells exhibit lower impedance than the LNMO-based cells, likely due to differences in morphology and surface area, as discussed above; ii) the scavenger-free cells including water-added electrolytes are more resistive since the presence of water leads to the formation of degradation products that affects the solid electrolyte interface;[18] iii) the dispersion of the functionalized alumina within the cathode further reduces the interfacial resistance compared to the Bare electrode, independently on the type of electrolyte used. Additionally, R_{CT} almost keeps stable at values lower than 20 Ω in case of C-ANP-cathodes (12 wt%), as shown in Figures S6 and S7 (Supporting Information) that report the

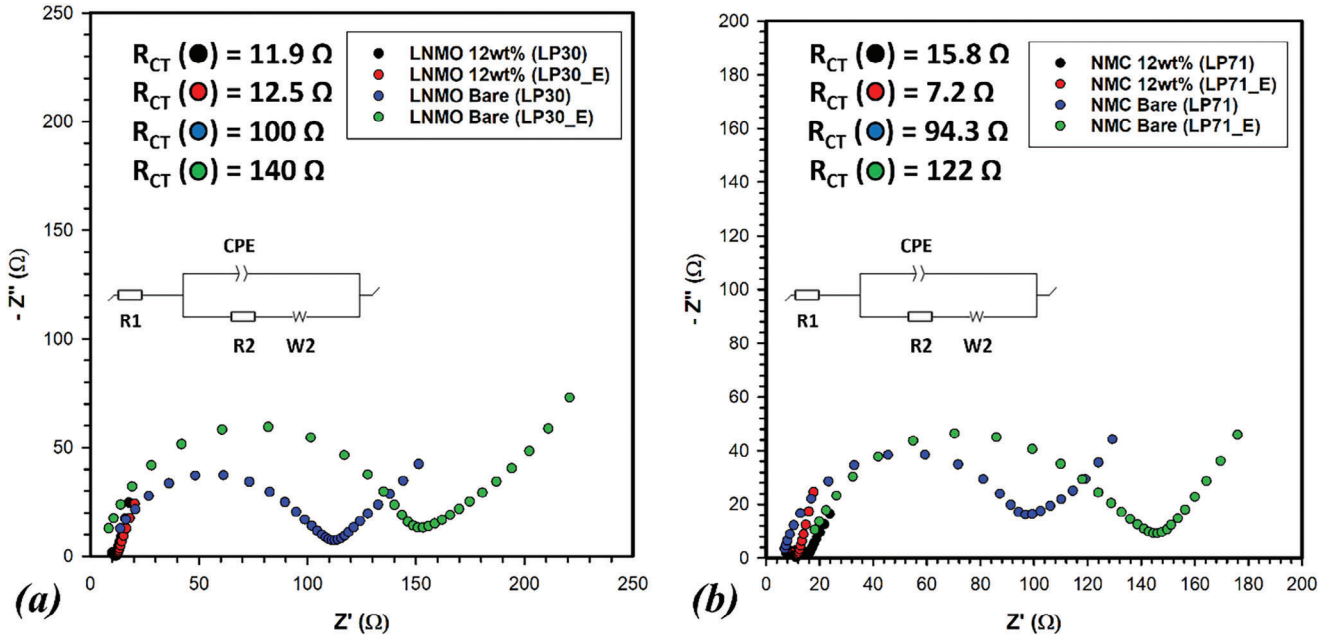

Figure 6. EIS plots were collected after 200 cycles for the a) LNMO- and b) NMC-based cathodes in the investigated cells.

impedance spectra evolution of LNMO- and NMC cells every 50 cycles at the end of the discharge half-cycle. This has been already observed in literature in case of Al_2O_3-coated $LiCoO_2$ cathodes and is interpreted in terms of effective capability of the filler to protect the cathode from decomposition reactions involving the electrolyte during the cycling process by hindering the formation of insulating passive layers.[46]

2.3. Post-Mortem Analysis

The structural and morphological evolution of the cathodes in a consequence of TMs dissolution was evaluated by means of XRD and SEM analysis, respectively. **Figure** 7a shows the XRD patterns of LNMO and LMNO with C-ANP cathodes before (@OCV) and after 200 cycles. The signal of Al collector, observed in all the patterns, was used as a reference to correct for any possible misalignment of the specimen, thus increasing the accuracy of the cell parameters determination of the electrode. The LNMO electrodes before the cycling tests show the expected spinel phase (cubic, space group *Fd*-3*m*, Figure S8a, Supporting Information), with a small fraction (3%) of a secondary rock salt phase likely corresponding to a mixed oxide composed of Li^+ and Mn^{3+} ions (see **Table** 2). The electrode keeps excellent structural stability over cycling, as proved by the cell parameters measured by Rietveld analysis that change only in order of 10^{-3} Å. The alumina signal is still preserved as very a small bump in the background, thus suggesting that no Al incorporation into the spinel phase took place. The XRD patterns of NMC cathodes are reported in Figure 7b. As for LNMO, the signal of Al collector, observed in all the patterns, was used as a reference. The pattern of the cathodes collected before cycling show the expected single-phase layered structure (rhombohedral, space group *R*-3*m*, $a \approx 2.88$ Å, $c \approx 14.20$ Å, see Figure S8b, Supporting Information). However, contrary to LNMO, some structural modifications are observed in the electrodes after 200 cycles, namely a minor cell expansion along the *c* axis, which might be related to the loss of TM ions in consequence of charging/discharging cycling (see Table 1).

Figure 8 shows the SEM images of all the investigated electrodes after long-term cycling of cells including pristine electrolytes (LP30, LP71) and water-enriched ones (LP30_E, LP71_E). By a comparison with the images of the cathode before the cycling experiment (see Figure 4), we notice that, in case of LNMO, no significant changes in the electrode surface morphology take placed upon cycling, independently on the used electrolyte. In contrast, the surface of the NMC-based cathodes without HF scavenger appears to be remarkably modified after the long-term test. Indeed, the NMC electrodes with 12wt% C-ANP exhibits a less damaged and more homogeneous surface after long-cycling, even in the presence of water-enriched electrolyte. This further demonstrates the higher activity of C-ANP as chemical barrier in case of the NMC systems.

Thermal behavior during abuse testing was finally evaluated for each cathode. **Figures** 9a,b show the ES-ARC overheating tests on Li/LNMO coin cells with both LP30 and LP30_E electrolytes and Li/NMC cells with LP71 and LP71_E electrolytes, respectively. These experiments enabled the determination of the maximum self-heating rate (*SHR*) and the critical temperature of exothermal phenomena (T_{exo}) indicating the cell decomposition and the related thermal runaway reactions.[49] LNMO-based cells exhibit similar temperatures for T_{exo}, ranging from 145 to 150 °C, except for the LNMO cell with LP71_E, where this occurs at a higher temperature of ≈172 °C (see **Table** 3). The *SHRs* values are reduced by the presence of functionalized alumina and increase when water added electrolyte is used (see Table 2). This is in nice agreement with what discussed in literature on the strongly detrimental influence of impurities and by-products

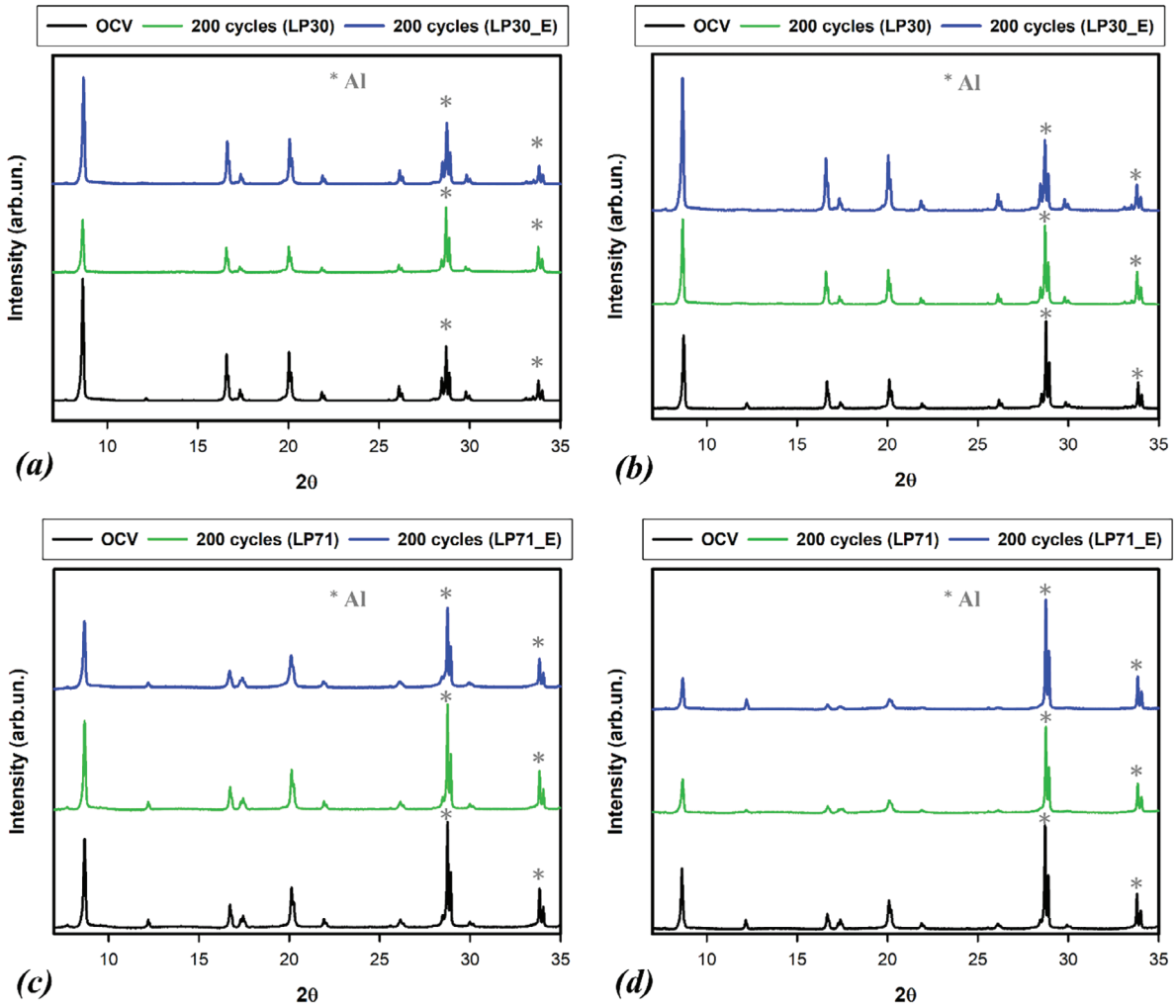

Figure 7. XRD patterns were collected for: a) LNMO, and b) LNMO 12wt% cathodes at the OCV and after 200 cycles the end of cycling with both LP30 and LP30_E; c) NMC Bare and d) NMC 12wt% cathodes at the OCV and at the end of cycling with both LP71 and LP71_E.

Table 2. Thermal properties of the investigated cathodes with and without C-ANP for both the electrolytes. T_{exo} and SHR: onset temperature of the exothermal phenomena and maximum self-healing rate detected in the ARC overheating tests; t_{MAX}: time to trigger the thermal runaway in the cells.

Samples	Electrolyte	TEXO [°C]	tMAX [min]	SH rateMAX [°C·min^{-1}]
LNMO Bare	LP30	150.7	1271	1.39
LNMO Bare	LP30_E	172.2	1125	1.738
LNMO 12wt%	LP30	155.7	1358	0.746
LNMO 12wt%	LP30_E	145.9	1248	1.114
NMC Bare	LP71	125.7 136.0	1140	1.738
NMC Bare	LP71_E	125.2 135.3	2246	3.032
NMC 12wt%	LP71	131.4 170.5	1290	1.347
NMC 12wt%	LP71_E	136.1	1286	1.375

of the electrolyte decomposition on the SHR process. The presence of C-ANPs hinders the generation of harmful and thermally degradable products in presence of water trace stabilising the cathode interface.[49,50]

In case of the NMC cathode, it is evident that the presence of C-ANP results in enhanced stability and lower *SHRs*. Specifically, for NMC 12wt% with LP71 and LP71_E, the measured *SHRs* were 1.347 and 1.375 °C min^{-1}, respectively, whereas the Bare cathode with the LP71 electrolyte achieved a significantly higher value of 1.738 °C min^{-1}. Additionally, two near-exothermic phenomena were observed at 125.7 and 136.0 °C, followed by a rapid thermal runaway. A separate discussion is required for the Bare cathode cell assembled with the water contaminated LP71_E, which shows a significantly different thermal behavior (Figure 9c). In this case, the coin cell underwent impressive swelling during the thermal runaway, reasonably due to release of gaseous decomposition by-products, leading to the very high *SHR* value of 3.032 °C min^{-1} (at least doubled with respect to the corresponding C-ANP cathode). As a result, the thermocouple used to read the sample self-heating parameter detached,

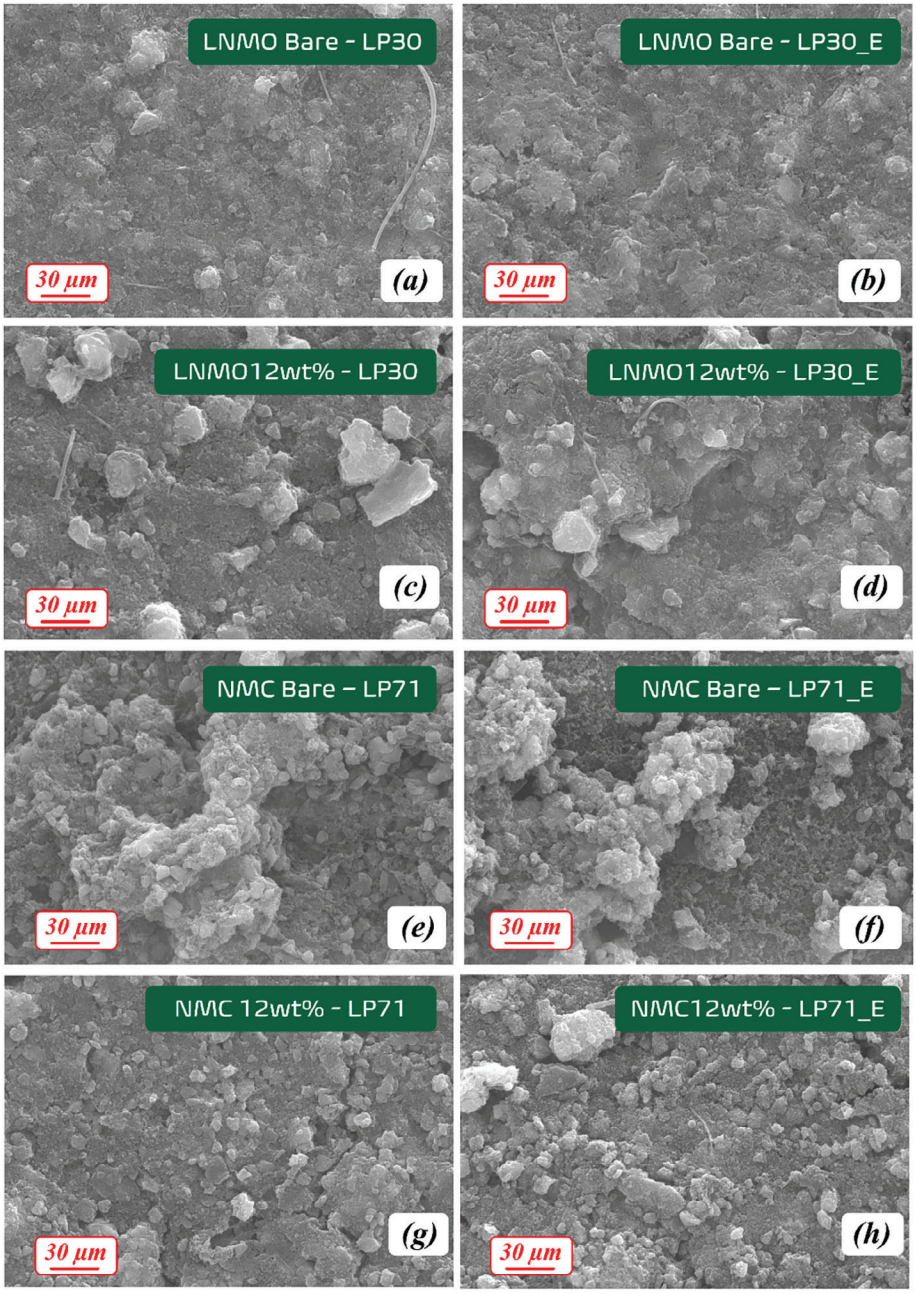

Figure 8. SEM images of the electrode surface after cycling are shown for: a,b) LNMO Bare and c,d) LNMO 12wt% of C-ANP with LP30 and LP30_E, respectively; for e,f) NMC Bare and g,h) NMC 12wt% of C-ANP with LP71 and LP71_E, respectively.

leading to an unreliable curve trend. The high *SHR* values recorded at the onset of the thermal runaway and the resulting volumetric expansion (recorded only during this case) indicate the lower stability of the cell with NMC and LP71_E as the electrolyte.

3. Conclusion

In this paper, we reported the synthesis and characterization of a hybrid organic-inorganic nanostructured scavenger for improving the stability of high-voltage cathode materials against degradation caused by HF in lithium-ion cells. The chitosan-decorated alumina nanoparticles showed an effective HF scavenging capacity even in the presence of significant amounts of water which promote electrolyte degradation. They also reduce the rate of dissolution of transition metals, without disturbing or altering the diffusion of the lithium ions during cell charge/discharge.

In addition, an improvement in cell safety was reported. Cathode materials encompassing the scavenger achieved better electrochemical performance with a significant reduction in capacity loss up to 200 cycles. Developments of the work could

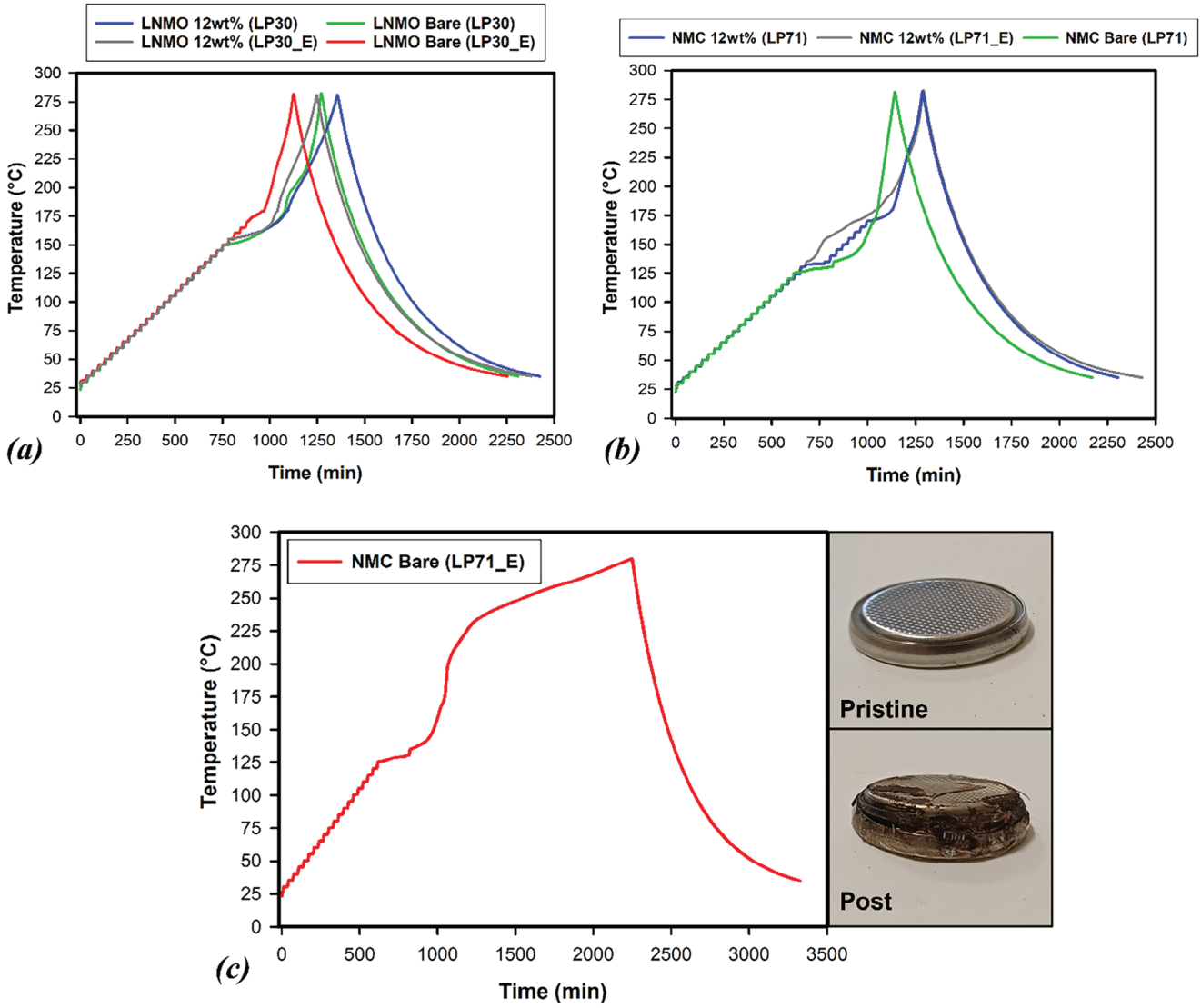

Figure 9. a) Thermal runaway behavior of the LNMO Bare and LNMO 12wt% of C-ANP cathodes when fully charged (at 4.9 V) using LP30 and LP30_E as electrolytes. b) Thermal runaway behavior of the NMC Bare, with LP71 and NMC 12wt% of C-ANP cathodes using LP71 and LP71_E as electrolytes, when fully charged at 4.6 V. c) Thermal runaway behavior of the NMC Bare, with LP71_E, fully charged at 4.6 V.

include the assembly of conjugated systems, able to perform scavenging activities toward different harmful species in the cell.

4. Materials and Methods

Synthesis of HF Scavenging C-ANPs: Alumina nanoparticles were synthesized by means of precipitation methods starting from aluminum nitrate nonahydrate ($Al(NO_3)_3 \bullet 9H_2O$) dissolved in methanol under magnetic stirring at room temperature until a transparent solution was obtained. Ammonium hydroxide solution (NH_4OH, 28.0–30.0% NH_3 basis) was then added dropwise to obtain a basic pH of 11–12. The resulting suspension was centrifugated at 6000 rpm for 40 min and the collected powder dried at 100 °C and then calcinated at 400 °C for 2 h.

The ANPs (200 mg) were dispersed in 20 mL of a chitosan solution in acetic acid (1 vol%) by constant stirring at room temperature for 2 h. The resulting nanocomposite was separated by centrifugation at 6000 rpm for 15 min and washed twice with distilled water to remove the excess of chitosan. The nanocomposite solution was finally dried overnight at 60 °C.

The scavenging activity of the C-ANPs was preliminary evaluated through an "*ex-situ*" approach to identify the optimal composition to use in the LNMO- and NMC-based cells. To this aim, pellets of the investigated cathode active materials (CAM = LNMO and NMC811) including different amounts of C-ANMs ranging from 0 to 12 wt% were dipped in commercial LP30 and LP71 electrolytes (see below), performing a 5-day treatment at 55 °C to promote HF formation by thermal decomposition. After that, the solution was analyzed by means of ICP-OES to determine the dissolution rate of the relevant TMs.

Cathode Preparation and Cell Assembly: The Bare cathode slurry was prepared by using 70 wt% of CAM (LNMO and

Table 3. Electrolytes employed and amount of water quantified using Karl-Fisher titration.

Electrolyte	Label	Water [ppm]
1 M $LiPF_6$ in EC:DMC (1:1)	LP30	50
1 M $LiPF_6$ in EC:DMC (1:1)–Added with water	LP30_E	170
1 M $LiPF_6$ in EC:DEC:DMC (1:1:1)	LP30	125
1 M $LiPF_6$ in EC:DEC:DMC (1:1:1)–Added with water	LP30_E	225

NMC811), 20 wt% of carbon black (Ensaco 350P, Imerys), and 10 wt% of a binder (polyvinylidene fluoride, PVDF). The solid content of the slurries was ≈28 wt%. Cathodic active materials and carbon powders were mixed in zirconia jars by a planetary ball mill at 150 rpm for 10 min twice, with a rest period of 5 min. The polymeric binder was then added and mixed with a similar procedure. The as prepared mixture was dispersed in N-methylpyrrolidone (NMP) (Sigma–Aldrich) to obtain the slurry, which was cast on a carbon-coated Al foil using a doctor blade with a wet thickness of 300 µm. The electrode was finally dried under vacuum at 80 °C to avoid any moisture and oxygen contamination. The cathode (active mass ≈3.0 mg cm^{-2}) was finally cut into 2 cm^2 disks and stored in an Ar-filled glove box (MBraun, H_2O, and O_2 < 0.5 ppm) before the electrochemical measurements. The same procedures were utilized for the realization of the scavenging cathode. In this case, a proper amount of C-ANPs (12 wt% with respect to the active material mass) was mixed with the components of the composite cathode before their dispersion in NMP.

All the functional tests were performed using a coin cell type (CR2032–MTI Corp.) assembled in glove box. Metallic Li was used as the counter electrode. A Whatman glass fiber, activated by 120–150 µL of liquid electrolyte, was used as the separator. Two different electrolyte solutions were used, depending on the CAM: i) 1.0 M $LiPF_6$ EC:DMC (1:1 v/v, LP30) in case of LNMO cathode; and ii) 1.0 M $LiPF_6$ EC:DEC:DMC (1:1:1 v/v, LP71) for NMC811. To evaluate the actual cathode scavenging ability, the electrolytes were added with a defined amount of water (120 ppm) to promote HF formation upon cycling. The exact water concentration in electrolytes (both pristine and water-contaminated) was measured by means of Karl Fischer titration and reported in Table 3. The scavenging activity was investigated by comparing the functional performances of LNMO and NMC cells (with both Bare and 12 wt% C-ANP cathode), including the pristine electrolytes (LP30 and LP71) and the water-enriched one (LP30_E) and LP71_E). To this aim, the chemical crosstalk of the dissolved transition metals was determined by measuring the concentration of Ni, Mn, and Co deposited at the Li anode after long-term cycling, as described in the following.

Characterization: XRD patterns were collected on a D8 Advance diffractometer (Bruker) equipped with Mo radiation in Bragg-Brentano configuration. The diffraction patterns for the CAMs and the composite cathodes (both before and after cycling) were collected in the 3°–38° for 2 h and 7°–35° for 3 h, 2θ ranges, respectively, with 0.01 deg. resolution.

The morphological and compositional characterization of the samples was performed with a Mira3XMU microscope (Tescan) operated at 20 kV and equipped with an EDAX EDX analysis system. The samples were coated with a carbon thin film using a Cressington 208 carbon coater.

A Spectrum Two FT-IR Spectrometer (PerkinElmer), with a MIR DTGS (deuterated triglycine sulfate) detector, equipped with Universal Attenuated Total Reflectance accessory (UATR) was used to collect the FTIR spectra of the scavenging filler. Four scans in the 4000–450 cm^{-1} range at 4 cm^{-1} resolution were coadded. Well ground powder samples were used, and the spectra were obtained after having pressed the samples on the ATR diamond crystal at room temperature. Peaks wavenumbers were attributed by using the "Labels" function of the Spectrum software.

ICP-OES analyses were performed by an Avio 220 max (Perkin Elmer), equipped with an AVIO Glass Cyclonic Baffled spray chamber, a quartz torch, and a dual backside-illuminated charge-coupled device (DBI-CCD) detector. The TMs quantification was carried out on HNO_3-digested solutions in the axial mode at 670.8 nm as wavelength, by an external standard calibration curve. ICP grade multi-elements standard (1000 mg L^{-1}, Merck) was diluted to 0.3–0.6–2.0–5.0–9.0 mg L^{-1} and then acidified to a final concentration of 2% nitric acid (from ultrapure 65% HNO_3, Merck). The measurement conditions were as in the following: nebulization gas flow: 0.7 L min^{-1}; power RF: 1500 W; auxiliary gas flow: 0.2 L min^{-1}; peristaltic pump: 1 mL min^{-1}; frequency: 500 Hz.

The electrochemical tests were performed by means of potentiodynamic electrochemical impedance spectroscopy (PEIS), galvanostatic cycling with potential limitation (GCPL), and potentiodynamic cycling with galvanostatic acceleration (PCGA) on coin cells assembled as described before. A battery tester Bio-Logic BCS-810 was used. PEIS scans between 10 kHz and 0.1 Hz were collected at 50 mV every 50 cycles by 2-electrode configuration cell to investigate the evolution of cell impedance upon cycling. Duplicate tests were conducted on cells with both the commercial electrolyte and the water-added electrolyte.

LNMO- and NMC811-based cells were cycled at 1C (theoretical capacity of 147 mAh g^{-1} ad 200 mAh g^{-1}, respectively) at room temperature in the voltage range 3.0–4.9 V for LMNO and 2.7–4.6 V for NMC. Two initial cycles at 0.25C, followed by two cycles at 0.5C, were carried out to allow the SEI formation and stabilization before the long cycling test.

The cell thermal stability was evaluated by performing Accelerated Rate Calorimetry (ARC-ES, Thermal Hazard Technology). Before the ARC test, the coin cells with NMC and LNMO cathodes were charged up to the limit voltage of 4.6 and 4.9 V, respectively, at a rate of 0.07 C and maintained at this voltage for 30 min. The accelerated rate calorimeter operated in a heat-wait-search (HWS) mode with a sensitivity threshold detection limit of 0.02 °C min^{-1}. The tests were performed in the temperature range of 30–280 °C, with a stepwise increase of 5 °C, and 15 min of equilibration time. If the temperature change rate exceeded 0.02 °C min^{-1}, the system switched to "exotherm mode", where self-heating occurs, and the coin cell could result in thermal runaway.

Supporting Information

Supporting Information is available from the Wiley Online Library or from the author.

Acknowledgements

The authors are grateful for the support of the MUR-PRIN "Healib" project funded by the European Union Next-GenerationEU. This study was carried out within the MOST–Sustainable Mobility Center and received funding from the European Union Next-GenerationEU (PIANO NAZIONALE DI RIPRESA E RESILIENZA (PNRR)–MISSIONE 4 COMPONENTE 2, INVESTIMENTO 1.4–D.D. 1033 17/06/2022, CN00000023). This manuscript reflects only the authors' views and opinions, neither the European Union nor the European Commission can be considered responsible for them.

Conflict of Interest

The authors declare no conflict of interest.

Data Availability Statement

Research data are not shared.

Keywords

HF, Lithium batteries, scavenger, self-healing, Transition Metal dissolution

Received: April 13, 2024
Revised: May 10, 2024
Published online: May 29, 2024

[1] Y. Cho, P. Oh, J. Cho, *Nano Lett.* **2013**, *13*, 1145.
[2] H. Zheng, Q. Qu, G. Zhu, G. Liu, V. S. Battaglia, H. Zheng, *ACS Appl. Mater. Interfaces* **2017**, *9*, 12445.
[3] L. Ben, H. Yu, Y. Wu, B. Chen, W. Zhao, X. Huang, *ACS Appl. Energy Mater.* **2018**, *1*, 8b01139.
[4] A. Du Pasquier, A. Blyr, P. Courjal, D. Larcher, G. Amatucci, B. Gérand, J. Tarascon, *J. Electrochem. Soc.* **1999**, *146*, 428.
[5] M. M. Thackeray, *Prog. Solid State Chem.* **1997**, *25*, 1.
[6] C. Zhan, T. Wu, J. Lu, K. Amine, *Energy Environ. Sci.* **2018**, *11*, 243.
[7] D. R. Gallus, R. Schmitz, R. Wagner, B. Hoffmann, S. Nowak, I. Cekic-Laskovic, R. W. Schmitz, M. Winter, *Electrochim. Acta* **2014**, *134*, 393.
[8] E. Billy, M. Joulié, R. Laucournet, A. Boulineau, E. De Vito, D. Meyer, *ACS Appl. Mater. Interfaces* **2018**, *10*, 16424.
[9] M. S. Whittingham, *Chem. Rev.* **2004**, *104*, 4271.
[10] W. Liu, P. Oh, X. Liu, M. Lee, W. Cho, S. Chae, Y. Kim, J. Cho, *Angew. Chem., Int. Ed.* **2015**, *54*, 4440.
[11] Y. Tesfamhret, H. Liu, Z. Chai, E. Berg, R. Younesi, *ChemElectroChem* **2021**, *8*, 1516.
[12] C. Zhan, T. Wu, J. Lu, K. Amine, *Energy Environ. Sci.* **2018**, *11*, 243.
[13] T. Nordh, R. Younesi, M. Hahlin, R. F. Duarte, C. Tengstedt, D. Brandell, K. Edström, *J. Phys. Chem. C* **2016**, *120*, 3206.
[14] J. Han, K. Kim, Y. Lee, N. Choi, *Adv. Mater.* **2019**, *31*, 1804822.
[15] C. Zhang, X. Lan, Q. Liu, L. Yu, Y. Li, X. Hu, *Mater. Today Phys.* **2022**, *24*, 100676.
[16] L. Mezzomo, C. Ferrara, G. Brugnetti, D. Callegari, E. Quartarone, P. Mustarelli, R. Ruffo, *Adv. Energy Mater.* **2020**, *10*, 2002815.
[17] B. Tang, N. Zhang, E. Alter, A. Eldesoky, J. R. Dahn, *J. Electrochem. Soc.* **2024**, *171*, 010518.
[18] K. Kim, H. Ma, S. Park, N.-S. Choi, *ACS Energy Lett.* **2020**, *5*, 1537.
[19] W. Li, C. Campion, B. L. Lucht, B. Ravdel, J. DiCarlo, K. M. Abraham, *J. Electrochem. Soc.* **2005**, *152*, A1361.
[20] J.-G. Han, M.-Y. Jeong, K. Kim, C. Park, C. H. Sung, D. W. Bak, K. H. Kim, K.-M. Jeong, N.-S. Choi, *J. Power Sources* **2020**, *446*, 227366.
[21] W. Xu, Y. Zheng, Y. Cheng, R. Qi, H. Peng, H. Lin, R. Huang, *ACS Appl. Mater. Interfaces* **2021**, *13*, 45446.
[22] B. Ziv, N. Levy, V. Borgel, Z. Li, M. D. Levi, D. Aurbach, A. D. Pauric, G. R. Goward, T. J. Fuller, M. P. Balogh, I. C. Halalay, *J. Electrochem. Soc.* **2014**, *161*, A1213.
[23] H. Bin Son, M. Shin, W.-J. Song, D.-Y. Han, S. Choi, H. Cha, S. Nam, J. Cho, S. Choi, S. Yoo, S. Park, *Energy Storage Mater.* **2021**, *36*, 355.
[24] R. Narayan, C. Laberty-Robert, J. Pelta, J. Tarascon, R. Dominko, *Adv. Energy Mater.* **2022**, *12*, 2102652.
[25] F. Mattelaer, P. M. Vereecken, J. Dendooven, C. Detavernier, *Adv. Mater. Interfaces* **2017**, *4*, 1601237.
[26] Z. Chen, Y. Qin, K. Amine, Y.-K. Sun, *J. Mater. Chem.* **2010**, *20*, 7606.
[27] X. Xiao, P. Lu, D. Ahn, *Adv. Mater.* **2011**, *23*, 3911.
[28] E. Carena, C. Colombo, C. Ferrara, R. Ruffo, P. Mustarelli, *Electrochem. Commun.* **2024**, *164*, 107728.
[29] S. Hildebrand, C. Vollmer, M. Winter, F. M. Schappacher, *J. Electrochem. Soc.* **2017**, *164*, A2190.
[30] S. Ito, S. Fujiki, T. Yamada, Y. Aihara, Y. Park, T. Y. Kim, S.-W. Baek, J.-M. Lee, S. Doo, N. Machida, *J. Power Sources* **2014**, *248*, 943.
[31] Y. Cho, Y.-S. Lee, S.-A. Park, Y. Lee, J. Cho, *Electrochim. Acta* **2010**, *56*, 333.
[32] C. Li, H. P. Zhang, L. J. Fu, H. Liu, Y. P. Wu, E. Rahm, R. Holze, H. Q. Wu, *Electrochim. Acta* **2006**, *51*, 3872.
[33] S. Yan, X. Sun, Y. Zhang, S. Fu, Y. Lang, L. Wang, G. Liang, *J. Solid State Chem.* **2022**, *306*, 122765.
[34] M. Aykol, S. Kim, V. I. Hegde, D. Snydacker, Z. Lu, S. Hao, S. Kirklin, D. Morgan, C. Wolverton, *Nat. Commun.* **2016**, *7*, 13779.
[35] D. Weber, Đ. Tripković, K. Kretschmer, M. Bianchini, T. Brezesinski, *Eur. J. Inorg. Chem.* **2020**, *2020*, 3117.
[36] Z. Chen, Y. Qin, K. Amine, Y.-K. Sun, *J. Mater. Chem.* **2010**, *20*, 7606.
[37] Y. Tesfamhret, R. Younesi, E. J. Berg, *J. Electrochem. Soc.* **2022**, *169*, 010530.
[38] K. Inoue, K. Yoshizuka, K. Ohto, *Anal. Chim. Acta* **1999**, *388*, 209.
[39] J. Roosen, S. Van Roosendael, C. R. Borra, T. Van Gerven, S. Mullens, K. Binnemans, *Green Chem.* **2016**, *18*, 2005.
[40] P. Sommi, A. Vitali, S. Coniglio, D. Callegari, S. Barbieri, A. Casu, A. Falqui, L. Vigano, B. Vigani, F. Ferrari, U. Anselmi-Tamburini, *ACS Nano* **2021**, *15*, 15803.
[41] T. Vegge, J. Tarascon, K. Edström, *Adv. Energy Mater.* **2021**, *11*, 2100362.
[42] Ľ. Smrčok, V. Langer, J. Křesťan, *Acta Crystallogr. C* **2006**, *62*, i83.
[43] J. Yan, J. Xu, S. Ai, K. Zhang, F. Yang, Y. Huang, *Arabian J. Chem.* **2020**, *13*, 5776.
[44] P. Li, Y. Wang, Z. Liu, X. Hu, *Mater. Chem. Front.* **2023**, *7*, 6318.
[45] S.-K. Hong, S.-I. Mho, I.-H. Yeo, Y. Kang, D.-W. Kim, *Electrochim. Acta* **2015**, *156*, 29.
[46] C. Xiong, H. Fu, L. Wu, G. Yuan, *Int. J. Electrochem. Sci.* **2020**, *15*, 8990.
[47] X. Li, J. Liu, X. Meng, Y. Tang, M. N. Banis, J. Yang, Y. Hu, R. Li, M. Cai, X. Sun, *J. Power Sources* **2014**, *247*, 57.
[48] Y. Tesfamhret, R. Younesi, E. J. Berg, *J. Electrochem. Soc.* **2022**, *169*, 010530.
[49] S. Ohneseit, P. Finster, C. Floras, N. Lubenau, N. Uhlmann, H. J. Seifert, C. Ziebert, *Batteries* **2023**, *9*, 237.
[50] F. Baakes, D. Witt, U. Krewer, *Chem. Sci.* **2023**, *14*, 13783.